A Nonvolatile Phase-Change Metamaterial Color Display

*Santiago García-Cuevas Carrillo, Liam Trimby, Yat-Yin Au, V. Karthik Nagareddy, Gerardo Rodriguez-Hernandez, Peiman Hosseini, Carlos Ríos, Harish Bhaskaran, and C. David Wright**

Chalcogenide phase-change materials, which exhibit a marked difference in their electrical and optical properties when in their amorphous and crystalline phases and can be switched between these phases quickly and repeatedly, are traditionally exploited to deliver nonvolatile data storage in the form of rewritable optical disks and electrical phase-change memories. However, exciting new potential applications are now emerging in areas such as integrated phase-change photonics, phase-change optical metamaterials/metasurfaces, and optoelectronic displays. Here, ideas from these last two fields are fused together to deliver a novel concept, namely a switchable phase-change metamaterial/metasurface resonant absorber having nonvolatile color generating capabilities. With the phase-change layer, here GeTe, in the crystalline phase, the resonant absorber can be tuned to selectively absorb the red, green, and blue spectral bands of the visible spectrum, so generating vivid cyan, magenta, and yellow pixels. When the phase-change layer is switched into the amorphous phase, the resonant absorption is suppressed and a flat, pseudowhite reflectance results. Thus, a route to the potential development is opened-up of nonvolatile, phase-change metamaterial color displays and color electronic signage.

1. Introduction

Chalcogenide phase-change materials, such as the well-known alloys $Ge_2Sb_2Te_5$ and GeTe, exhibit a pronounced difference in their electrical and optical properties between their amorphous and crystalline phases. Moreover, they can be switched (optically, electrically, or thermally) between phases reversibly (potentially $>10^{15}$ cycles) and quickly (nanoseconds or faster).[1–3] Both phases (and indeed intermediate phases between fully crystalline and fully amorphous) are also stable at room temperature for a time on the order of years.[4,5] All these properties have made phase-change materials extremely attractive for commercial data storage technologies, in the form of rewritable optical disks and nonvolatile electronic memories.[6–8] More recently, as a result of the rather unique properties that phase-change materials possesses, their use has been extended to a number of exciting emerging applications including neuromorphic computing,[9,10] integrated photonic memories[11,12] and, the focus of this work, reconfigurable optical metamaterials/metasurfaces,[13–22] which we here exploit for the realization of a new form of nonvolatile color display.

Optical metasurfaces have great potential to generate color, and several different structures suited to this task have been suggested in the literature.[23–31] A common approach is to utilize metallic (or metal-dielectric) nanorods[26,27,30,31] or other lithographically patterned metal-dielectric nanostructures[24,28,29] that generate structural (i.e., noncolorant) color using plasmonic effects. Such approaches are in general though "fixed-by-design," meaning that colors and images are essentially written permanently into the metasurface by the specific nanostructures used. For display and electronic signage applications, however, the ability to change the displayed image or information in real time is required. Here we provide just such a capability by combining a metal-insulator-metal (MIM) resonant absorber type optical metasurface[32,33] with a thin layer of chalcogenide phase-change material (PCM), so providing the key attributes of nonvolatile color generation and dynamic reconfigurability, the latter achieved by turning the MIM resonance "on" and "off" by switching the PCM-layer between its crystalline and amorphous states. Nonvolatility is a particularly attractive feature offered by phase-change based displays, since no power is needed to retain an image once it is written into the phase-change layer/pixels.[34–37] Moreover, the displays can work using only ambient (natural or artificial) light, which can

S. G.-C. Carrillo, L. Trimby, Dr. Y.-Y. Au, Dr. V. K. Nagareddy, Prof. C. D. Wright
Department of Engineering
University of Exeter
Exeter EX4 4QF, UK
E-mail: David.Wright@exeter.ac.uk
Dr. C. Ríos, Prof. H. Bhaskaran
Department of Materials
University of Oxford
Oxford OX1 3PH, UK
Dr. G. Rodriguez Hernandez, Dr. P. Hosseini
Bodle Technologies Ltd.
Begbroke Science Park, Oxford OX5 1PF, UK
The ORCID identification number(s) for the author(s) of this article can be found under https://doi.org/10.1002/adom.201801782.

DOI: 10.1002/adom.201801782

also significantly reduce power consumption; indeed, contrary to conventional display technologies, the images generated in displays such as that presented here will appear brighter if the intensity of the incident light shining on them increases–another attractive feature. There are thus many exciting application possibilities for phase-change displays, including mobiles, smart labeling, in-window displays, IoT devices, wearables, near-eye displays, and even artificial retinas.

2. Device Design and Working Principle

The basic structure of our phase-change material-based MIM metamaterial absorber is shown in **Figure 1**a. The absorber stack is composed of an aluminum bottom plane, a layer of GeTe, a layer of indium tin oxide (ITO), and a top aluminum layer patterned into circles. We chose aluminum for the metal layers due to its good plasmonic behavior that extends down to visible wavelengths, as well as its ease of incorporation into standard semiconductor manufacturing processes.[17,38,39] The ITO layer provides environmental protection for the PCM layer (since chalcogenides readily oxidize in air[40]), while of course being transparent (necessary to sustain the absorber's resonant mode) due to its low absorption coefficient at visible wavelengths. GeTe is used for the PCM layer since it presents very interesting properties in the visible spectrum, properties that can be used to tune the response of MIM absorbers. Specifically, the negative value of the real part of the permittivity of GeTe in the crystalline phase indicates an optically metallic-like behavior;[41,42] such behavior is used here to support and confine a resonant mode primarily in the ITO layer for a specific (user-defined) spectral band. As a result, the energy that corresponds to the wavelengths that fulfill the resonant condition will be absorbed. On the other hand, the optical constants of GeTe in the amorphous phase are more similar to those of a lossy dielectric; thus, when the GeTe layer is switched to the amorphous state, the absorber's resonant condition cannot be fulfilled, resulting in an essentially flat reflectance spectrum (see the Supporting Information). The structure of Figure 1a is thus ideally suited to the generation of color using resonant absorption: with the GeTe layer in the crystalline phase, the structure is designed (by proper choice of the resonator geometric parameters–see later) to absorb in the red, green, and blue (RGB) wavebands, so generating cyan, magenta, and yellow (CMY) pixels respectively; with the GeTe layer amorphous, the resonant absorption is switched off and a

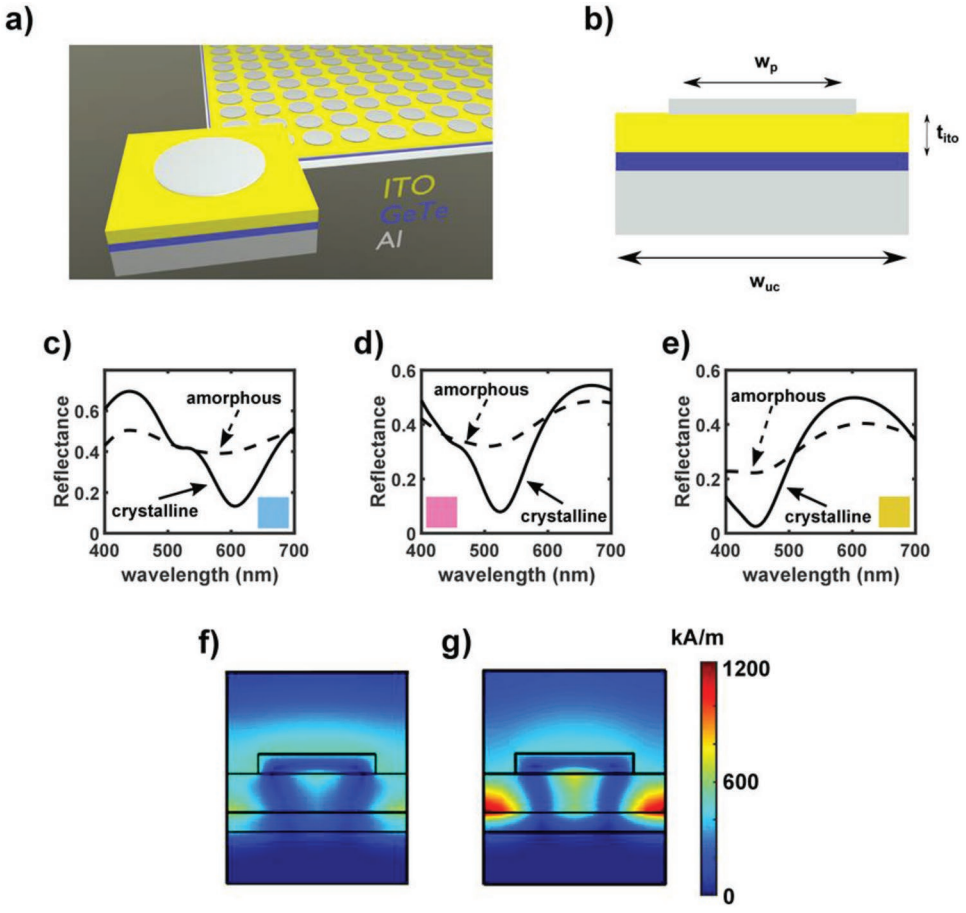

Figure 1. a) 3D schematic of the phase-change MIM absorber structure and the materials used. b) Cross sectional view of the structure with labeling of the geometrical parameters varied in the optimization of the devices. c–e) Optimized reflectance spectra of the (c) cyan, (d) magenta, and (e) yellow pixels, as obtained by FEM simulation. f,g) Magnitude of the magnetic field (in the direction perpendicular to the plane) in the MIM absorber with the GeTe layer in the amorphous (f) and crystalline (g) phase.

white-like reflectance should be obtained. By such means a full color palette should be attainable using standard subtractive color techniques.[31,43,44]

The response of the MIM absorber of Figure 1a is controlled (designed) by the width (diameter) of the top metallic resonator (w_p), the width (w_{uc}) of the unit cell (i.e., the periodicity of the structure), and the thickness of the ITO layer (t_{ito}), see Figure 1b. The thicknesses of the aluminum bottom plane, the GeTe layer and the top metal layer are fixed in our approach, at 80, 30, and 30 nm respectively: the bottom aluminum layer being chosen to be thick enough to prevent any radiation passing through the structure; the GeTe thickness being chosen thin enough to facilitate effective (electrical, thermal, or optical) switching of the phase-state, while being thick enough to present sufficient optical contrast between states; the top aluminum layer is thick enough to prevent significant deviation of the optical constants from those of the bulk while at the same time is thin enough to provide a good lithographic process facilitating lift-off. At resonance, a gap plasmon[33] is excited in the MIM absorber and currents in the top metal resonator are mirrored in the bottom metal plane, resulting in the excitation of a transversal magnetic resonant mode. This mode is, in our case, essentially a magnetic dipole below the top resonator and transversal to the polarization direction of the incident electric field (see the Supporting Information for a more detailed discussion of the resonant modes in the structure). If the structure is properly designed, the incident radiation can be perfectly coupled to the resonant mode, resulting in near-zero reflectance at the resonant wavelength/frequency, which is here chosen to coincide with the center of the RGB wavebands, so generating, at resonance, CMY pixels.

The workflow for designing the different pixels starts with a parametrization of the geometric distances that mainly determine the performance of the MIM device, i.e., w_p, w_{uc}, and t_{ito}, (see Figure 1b). The reflectance spectra of the designed MIM structures are then calculated at visible wavelengths using finite element modeling (FEM). We use an equal energy illuminant (E illuminant), although any other illuminant profile could have been used (and the choice will depend on illumination conditions for which we want an optimal performance of the device). Once an appropriate reflectance spectrum is achieved, colorimetric calculations are carried out to quantify the performance of the device in terms of color production (see the Supporting Information for further details on the reflectance spectra and colorimetric calculations). Once we have a geometrical representation, as points on the standard CIE 1931 chromaticity diagram, of the MIM reflectance spectra (with the GeTe layer in both crystalline and amorphous states), we run a further optimization algorithm on the structure that minimizes the distance between these points and those for "ideal" CMY pixels (the latter chosen according to the "Specifications for Web Offset Publications"[45]). We use a pattern search algorithm, in the Global Optimization Toolbox in Matlab, to find the optimum geometry that makes the points corresponding to the calculated spectra to be as close as possible to their respective chosen objectives.

Following the above approach, the calculated reflectance spectra corresponding to the optimal phase-change MIM absorber structure for cyan, magenta, and yellow pixels are shown in Figure 1c–e, respectively. It can be seen that these reflectances are indeed characterized by a strong absorption in the red, green, and blue wavebands when the GeTe layer is crystalline, but by a nearly flat response when the GeTe layer is amorphous. We earlier attributed the resonant behavior and the subsequent absorption (with the GeTe in the crystalline state) to a better confinement of the resonant mode in the ITO layer. This is indeed the case, as can be seen in Figure 1f,g where the distribution of the modulus of the magnetic field (perpendicular to the plane of the paper) is shown for the magenta pixel at 520 nm excitation wavelength and with the GeTe layer amorphous (Figure 1f) and crystalline (Figure 1g). The field amplitudes are much higher when GeTe is crystalline, and the effective confinement of the field to the ITO layer is clear. This is precisely what we should expect following our discussion in the previous sections on the operation of the MIM structure and the optical constants of GeTe. Note that the MIM dimensions yielding the CMY responses of Figure 1 are given in **Table 1**.

Table 1. Geometrical parameters for the optimized phase-change MIM type cyan, magenta, and yellow pixels (all dimensions in nm).

Pixel type	w_{uc}	w_p	t_{ito}
Cyan	329	214	84
Magenta	278	181	60
Yellow	240	156	37

3. Results and Discussion

Having successfully designed and simulated suitable CMY pixels using our phase-change MIM absorber approach, we now report on their experimental realization. The requisite structures for each pixel color were fabricated using magnetron sputtering to deposit the stack of layers (i.e., the Al, GeTe, and ITO layers) on a Si/SiO_2 substrate, followed by electron-beam lithography to define the top resonator pattern (carried out using a PMMA mask followed by sputter deposition of the top Al layer and lift-off–see the Experimental Section for further details). Scanning electron microscope (SEM) images of typical as-fabricated structures are shown for each pixel color in **Figure 2**a–c along with, inset, the actual colors generated by the experimental pixels with the GeTe layer in the amorphous and crystalline phases. Figure 2a–c reveals that the target dimensions of the top resonator pattern (as in Table 1) match very closely those actually achieved. Moreover, with GeTe in the crystalline phase the desired CMY colors are produced and, with the GeTe amorphous, a more white-like response is obtained. A more quantitative evaluation of the colors produced can be however obtained by measurement of the reflectance spectra and by mapping to the standard CIE color diagram, both of which we report below.

The reflectance spectra of the as-fabricated phase-change MIM structures were measured using a microspectrophotometer (see the Experimental Section for details). Once we obtained the data corresponding to the as-deposited amorphous phase of the GeTe, we crystallized the GeTe by heating to 250 °C for 15 min and remeasured the spectra. The results

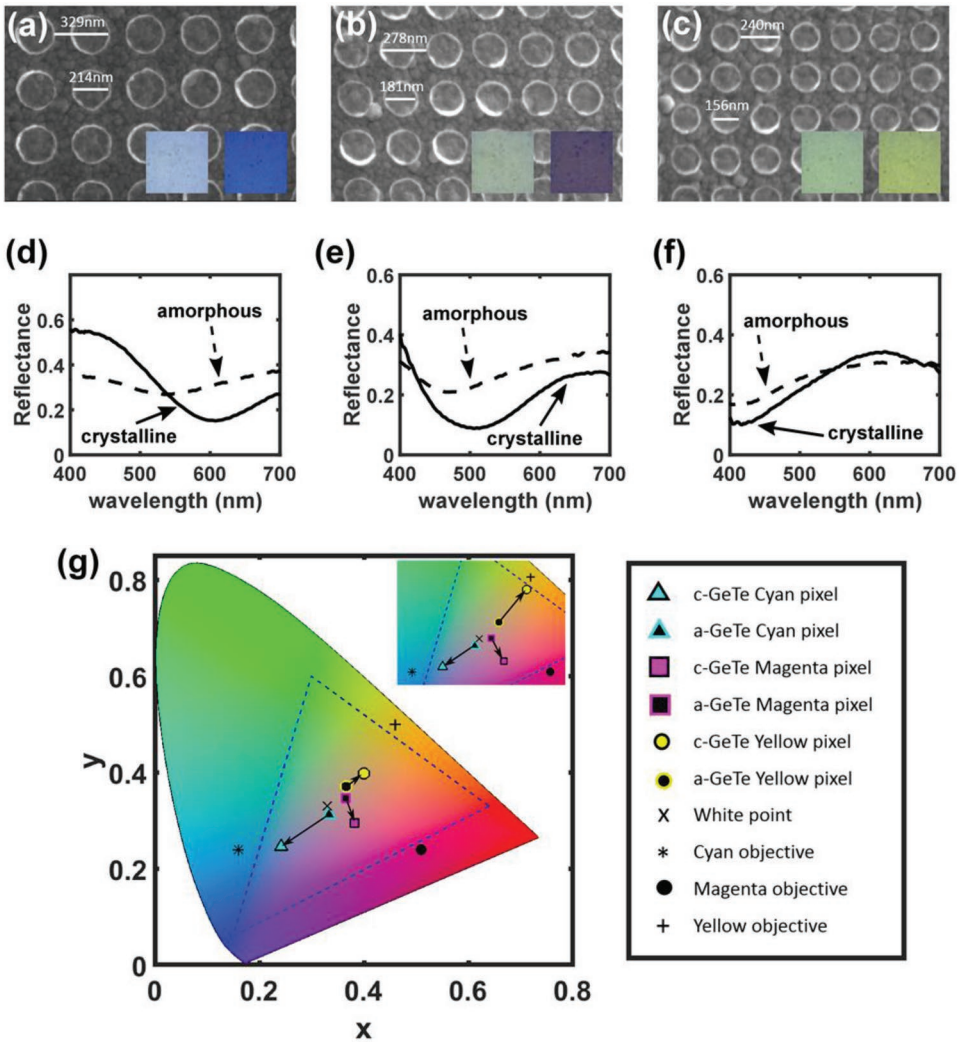

Figure 2. SEM images of the as-fabricated phase-change MIM a) cyan, b) magenta, and c) yellow pixel structures. The insets are optical microscope images that clearly show the colors generated with the GeTe layer in both the amorphous (left) and crystalline (right) states. d,e,f) Experimental reflectance spectra for the cyan, magenta, and yellow pixels, respectively. g) Representation of the spectra in (d,e,f) in the CIE 1931 chromaticity space (inset shows the mapping of the FEM simulated pixel responses of Figure 1). Also shown are additional aspects of interest, such as color objective points, with the relevant legend adjacent to the CIE 1931 diagram.

are shown in Figure 2d–f and show the expected preferential absorption (with GeTe crystalline) in the RGB wavebands for the CMY pixels, respectively. These measured spectra were then mapped to the CIE 1931 chromaticity diagram, as shown in Figure 2g (where, for comparison purposes, we also show, inset, the mapping of the colors simulated via FEM). We observe a good performance for the experimental cyan and magenta pixels when compared with the simulated behavior. However, when the MIM absorption peak moves to blue wavelengths (≈420 nm), so producing a yellow color, the agreement between the experimental and simulated pixels is not so strong. This is most likely due to the fact that the blue MIM absorber has the smallest feature sizes and so imperfections in the fabrication process (e.g., film roughness) have a greater influence on performance. Such imperfections, as well as uncertainties in the optical constants of the various layers in the devices, are most likely the cause of differences seen in the simulated (Figure 1) and experimental (Figure 2) reflectance spectra. A closer correlation between the simulated (i.e., designed) performance and that achieved experimentally is thus expected for tightly-characterized films and optimized deposition conditions (e.g., to reduce roughness).

We now turn our attention to the generation of display information and images using the phase-change MIM pixels designed and fabricated above. For fixed displays, such as permanent or semi-permanent signage/advertising/notifications, the vivid color differences obtained using the CMY pixels (i.e., with the GeTe layer fixed in the crystalline state) could prove very useful. This is illustrated in **Figure 3**a,b where a simple warning display is generated using combinations of cyan/magenta pixels (Figure 3a) and cyan/yellow pixels (Figure 3b); images were generated from simulated and experimental reflectance spectra (i.e., the spectra shown in Figure 1c–e and Figure 2d–f respectively), see the Supporting Information for

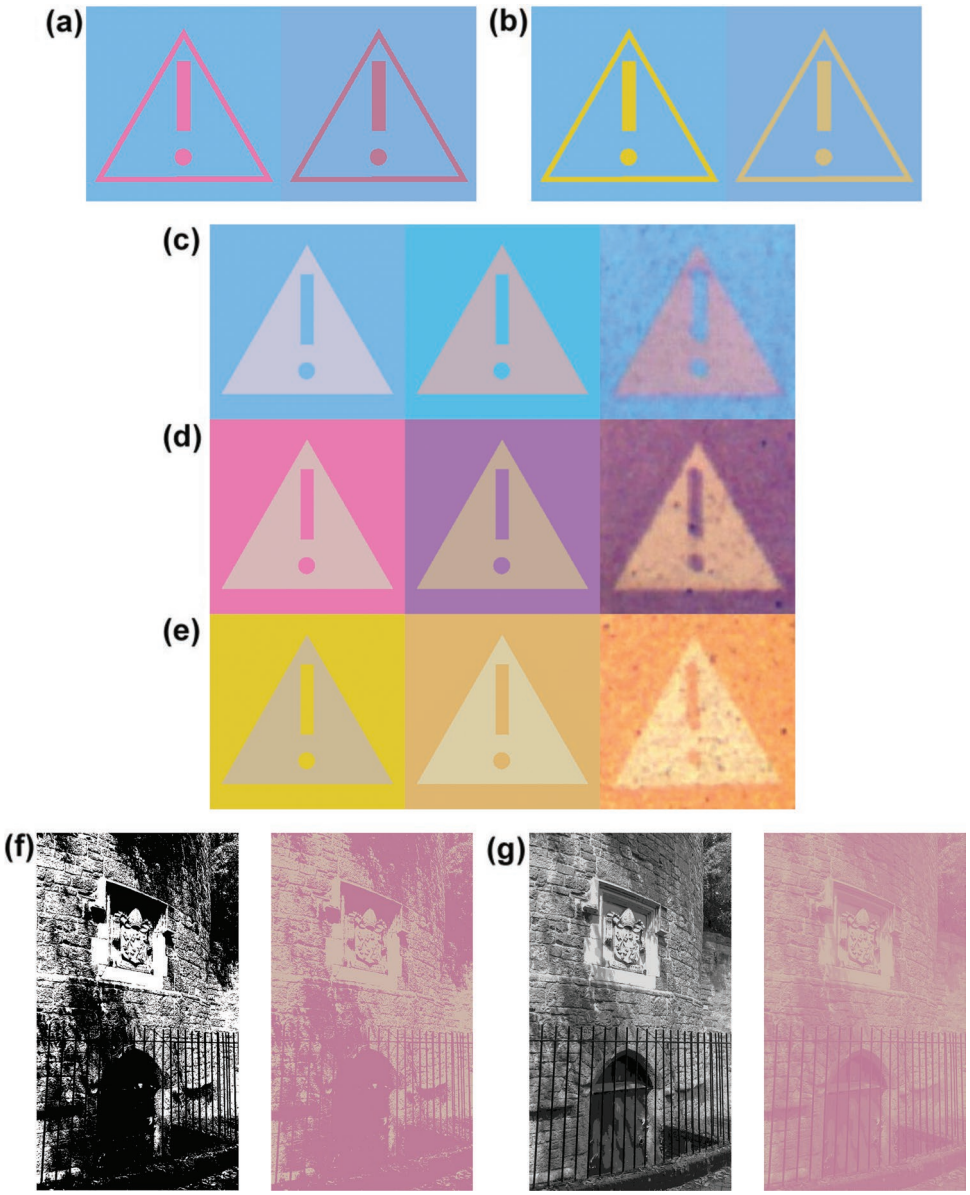

Figure 3. Phase-change MIM image generation. a,b) Images produced by a fixed arrangement of two differently colored phase-change MIM pixels with the GeTe layer in the crystalline phase; (a) uses cyan and magenta pixels, (b) cyan and yellow pixels. Shown in each case are (left) images produced using spectral data from FEM simulations and (right) images generated using experimental spectral data. c,d,e) Images in CMY pixels and with the warning triangle being produced by GeTe in its amorphous phase and the background and exclamation mark by crystalline GeTe. In each of (c,d,e) we show the image generated using simulated spectra (left), experimental spectra (middle) and the image experimentally written in the pixel (right), for the C, M, and Y cases, respectively. f) A binary (black and white) image of part of Exeter's city wall (left), rendered to a binary image using magenta pixels (right) with the GeTe layer in both crystalline (for the black regions) and amorphous (for the white) phases. g) An 8-level gray-scale version of the city wall (left), rendered to an 8-level image in magenta pixels (right), using fractional crystallization of the GeTe layer.

more details. The advantage of using the phase-change MIM approach for such fixed displays is that the color is essentially structurally generated and so, unlike colorant-based displays, is not subject to any fading with age or extended exposure to sunlight. Moreover, the stronger the ambient illumination, the stronger the resulting image contrast, unlike the case for many conventional electronic displays.

Of course, since the GeTe layer can be switched between phases, by for example using electrical or thermal excitation,[34,46] we are not limited to the generation of fixed displays. By way of an example we show in Figure 3c–e the same image as that of Figure 3a,b but in this case rendered into a single pixel type (cyan, magenta, and yellow) and with the warning triangle displayed using the GeTe layer in its amorphous state and the background and exclamation mark by the GeTe in the crystalline state. For each pixel type in Figure 3c–e we show the images generated using the simulated spectra from Figure 1, from the experimentally measured spectra of

the fabricated devices and from actual experimental images written using a scanning laser to switch the phase of the GeTe layer in the sample. (see Section S6 in the Supporting Information for details of the experimental image writing process, and for a detailed discussion of practicable approaches to phase-switching in phase-change meta-absorber type devices of the type discussed here–and the potential impact that the phase-switching approach used will have on the choice of suitable materials for the top and bottom metal layers). It can be seen, that, in general, the agreement between simulated and experimental colors is quite good, and that the experimentally written images are bright and vivid in color. Confirmation that regions shown in the images of Figure 3c–e were indeed amorphous (for the triangle) and crystalline (for the background and exclamation mark) was obtained using Raman analysis, see the Supporting Information.

Next, we demonstrate some of the potentialities of phase-change MIM type pixels for the display of more complex image information. Thus, in Figure 3f we show a binary (black and white) image of part of Exeter's city wall, rendered into a binary image in a phase-change MIM display, here using magenta pixels with the GeTe layer in either crystalline or amorphous states. In Figure 3g we show an 8-level gray-scale version of the city wall, rendered into an 8-level image in the phase-change MIM display, again in this case using magenta pixels. Note that the 8-levels of contrast are here attained by assuming the GeTe layer can be switched into 8 different fractionally-crystallized states; since chalcogenide phase-change memories have been shown capable of being switched to multiple levels,[8,47] such an assumption is reasonable. Such a gray-scale display could find utility in emerging applications such as wearable electronics, where there is a need to display basic information in a cheap and simple way and under a wide variety of ambient light conditions. However, it should be noted that, as demonstrated via the color map of Figure 2g, our phase-change MIM displays are not limited to simple binary or gray-scale color generation. Indeed, pixels could be combined in various arrangements to form new palettes richer in color.

Finally, we look beyond display type technologies and point out that phase-change MIM absorber structures of the form developed in this work may also find applications in another interesting field. To do this we consider the operation of the devices not from the reflection point of view, but instead from the absorption point of view. As pointed out in the previous sections, our devices have the ability to modulate light absorption in the red, green, and blue spectral bands. This type of behavior is intimately related to human visual perception, specifically with the cone cells located in the retina and responsible for color perception. Thus, it may well be that devices of the type presented here can offer new and interesting possibilities in biologically-inspired artificial vision systems or visual prostheses.[48,49]

4. Conclusions

In summary, we have demonstrated how it is possible, as a result of the combination of chalcogenide phase-change materials and metamaterial absorber structures, to create a novel tunable CMY-based optoelectronic color generation system. With the phase-change layer, here GeTe, in the crystalline phase, the resonant absorber can be tuned to selectively absorb the red, green, and blue spectral bands of the visible spectrum, so generating vivid cyan, magenta, and yellow pixels. When the phase-change layer is switched into the amorphous phase, the resonant absorption is suppressed and a flat, pseudo-white reflectance results. Our approach has the advantages of being nonvolatile, fast, inexpensive, and suitable for use in a wide range of ambient light conditions, including bright sunlight. There are thus many attractive potential applications for such displays, including mobiles, smart labeling, in-window displays, IoT devices, wearables, near-eye displays, and even, possibly, artificial retinas.

5. Experimental Section

The stack of layers Al/GeTe/ITO used in the display pixel structure was deposited via magnetron sputtering without breaking the vacuum for each individual device. The top patterned aluminium layer was fabricated with a conventional e-beam lithography process using a mask of PMMA followed by magnetron sputtering and lift-off of the mask. A 200 nm layer of PMMA 950K A4 was spun on the substrates with the deposited stack of layers and baked at 100 °C for 10 min (a temperature low enough to prevent crystallization of GeTe, which as-deposited is in the amorphous phase). The pattern was written using an e-beam current of 1.4 nA and a dose of 7 C m^{-2}. The development mixture was composed of IPA:MIBK:MEK 15:5:1 solution and development was for 35 s at room temperature. Finally, aluminum was sputtered in the prepared mask. The lift-off process consisted of a bath of acetone at 60 °C for 2 h followed by a mild sonication.

The optical reflectance spectra were obtained using a Jasco MSV-5300 UV–vis/NIR microspectrophotometer using a 20× objective with 0.3 numerical aperture. The crystallization of the GeTe layer for spectral characterization was carried out by thermal annealing at 250 °C for 15 min.

Raman measurements, for confirmation of crystallization when experimentally rendering images into the pixels (see Section S7 in the Supporting Information), were acquired in a backscattering configuration using a Horiba confocal Raman microscope operating at 532 nm and equipped with an air-cooled charge coupled device (CCD) detector.

Supporting Information

Supporting Information and data is available from the Wiley Online Library or from the author.

Acknowledgements

S.G.-C.C. acknowledges funding via the EPSRC CDT in Metamaterials (EP/L015331/1). H.B. and C.D.W. acknowledge funding via the EPSRC ChAMP and WAFT grants (EP/M015130/1 and EP/M015173/1). C.D.W. and V.K.N. acknowledge funding support via grant #N62909-16-1-2174 from the Office of Naval Research Global (ONRG).

Conflict of Interest

Gerardo Rodriguez-Hernandez, Peiman Hosseini, and Harish Bhaskaran are either employed or work in an executive capacity for Bodle

Technologies Ltd. C. David Wright is an advisor to Bodle Technologies Ltd. Hosseini, Bhaskaran, Wright, and Carrillo have patents or patent applications relating to phase-change displays.

Keywords

active metasurfaces, chalcogenide phase-change devices, metamaterial displays, phase-change displays

Received: December 20, 2018
Revised: March 1, 2019
Published online:

[1] I. S. Kim, S. L. Cho, D. H. Im, E. H. Cho, D. H. Kim, G. H. Oh, D. H. Ahn, S. O. Park, S. W. Nam, J. T. Moon, C. H. Chung, in *2010 Symp. on VLSI Technology*, IEEE, Piscataway, NJ **2010**, pp. 203–204.
[2] M. Wuttig, H. Bhaskaran, T. Taubner, *Nat. Photonics* **2017**, *11*, 465.
[3] D. Loke, T. H. Lee, W. J. Wang, L. P. Shi, R. Zhao, Y. C. Yeo, T. C. Chong, S. R. Elliott, *Science* **2012**, *336*, 1566.
[4] S. Raoux, M. Wuttig, *Phase Change Materials: Science and Applications*, Springer, New York **2009**.
[5] S. Raoux, W. Wełnic, D. Ielmini, *Chem. Rev.* **2010**, *110*, 240.
[6] M. Wuttig, N. Yamada, *Nat. Mater.* **2007**, *6*, 824.
[7] S. Raoux, F. Xiong, M. Wuttig, E. Pop, *MRS Bull.* **2014**, *39*, 703.
[8] G. W. Burr, M. J. BrightSky, A. Sebastian, H.-Y. Cheng, J.-Y. Wu, S. Kim, N. E. Sosa, N. Papandreou, H.-L. Lung, H. Pozidis, E. Eleftheriou, C. H. Lam, *IEEE J. Emerging Sel. Top. Circuits Syst.* **2016**, *6*, 146.
[9] Z. Cheng, C. Ríos, W. H. P. Pernice, C. D. Wright, H. Bhaskaran, *Sci. Adv.* **2017**, *3*, e1700160.
[10] C. D. Wright, P. Hosseini, J. A. V. Diosdado, *Adv. Funct. Mater.* **2013**, *23*, 2248.
[11] C. Ríos, M. Stegmaier, P. Hosseini, D. Wang, T. Scherer, C. D. Wright, H. Bhaskaran, W. H. P. Pernice, *Nat. Photonics* **2015**, *9*, 725.
[12] M. Stegmaier, C. Ríos, H. Bhaskaran, W. H. P. Pernice, *ACS Photonics* **2016**, *3*, 828.
[13] S. García-Cuevas Carrillo, G. R. Nash, H. Hayat, M. J. Cryan, M. Klemm, H. Bhaskaran, C. David Wright, *Opt. Express* **2016**, *24*, 13563.
[14] C. de Galarreta, A. M. Alexeev, A. Yat-Yin, M. Lopez-Garcia, M. Klemm, M. Cryan, J. Bertolotti, C. D. Wright, *Adv. Funct. Mater.* **2018**, *28*, 1704993.
[15] N. I. Zheludev, Y. S. Kivshar, *Nat. Mater.* **2012**, *11*, 917.
[16] B. Gholipour, J. Zhang, K. F. MacDonald, D. W. Hewak, N. I. Zheludev, *Adv. Mater.* **2013**, *25*, 3050.
[17] A. Tittl, A.-K. U. Michel, M. Schäferling, X. Yin, B. Gholipour, L. Cui, M. Wuttig, T. Taubner, F. Neubrech, H. Giessen, *Adv. Mater.* **2015**, *27*, 4579.
[18] Q. Wang, E. T. F. Rogers, B. Gholipour, C.-M. Wang, G. Yuan, J. Teng, N. I. Zheludev, *Nat. Photonics* **2016**, *10*, 60.
[19] Y. Chen, X. Li, X. Luo, S. A. Maier, M. Hong, *Photonics Res.* **2015**, *3*, 54.
[20] Y. Chen, X. Li, Y. Sonnefraud, A. I. Fernández-Domínguez, X. Luo, M. Hong, S. A. Maier, *Sci. Rep.* **2015**, *5*, 8660.
[21] Y. G. Chen, T. S. Kao, B. Ng, X. Li, X. G. Luo, B. Luk'yanchuk, S. A. Maier, M. H. Hong, *Opt. Express* **2013**, *21*, 13691.
[22] A. Nemati, Q. Wang, M. Hong, J. Teng, *Opto-Electron. Adv.* **2018**, *1*, 18000901.
[23] Y.-K. R. Wu, A. E. Hollowell, C. Zhang, L. J. Guo, *Sci. Rep.* **2013**, *3*, 1194.
[24] F. Cheng, J. Gao, T. S. Luk, X. Yang, *Sci. Rep.* **2015**, *5*, 11045.
[25] Y. Yu, L. Wen, S. Song, Q. Chen, *J. Nanomater.* **2014**, *2014*, 1.
[26] K. Kumar, H. Duan, R. S. Hegde, S. C. W. Koh, J. N. Wei, J. K. W. Yang, *Nat. Nanotechnol.* **2012**, *7*, 557.
[27] G. Si, Y. Zhao, J. Lv, M. Lu, F. Wang, H. Liu, N. Xiang, T. J. Huang, A. J. Danner, J. Teng, Y. J. Liu, *Nanoscale* **2013**, *5*, 6243.
[28] T. Xu, Y.-K. Wu, X. Luo, L. J. Guo, *Nat. Commun.* **2010**, *1*, 1.
[29] A. S. Roberts, A. Pors, O. Albrektsen, S. I. Bozhevolnyi, *Nano Lett.* **2014**, *14*, 783.
[30] J. K. W. Tan, S. J. Zhang, L. Zhu, D. Goh, X. M. Qiu, C-W. Yang, *Nano Lett.* **2014**, *14*, 4023.
[31] S. D. Rezaei, J. Ho, R. J. H. Ng, S. Ramakrishna, J. K. W. Yang, *Opt. Express* **2017**, *25*, 27652.
[32] Y. Cui, Y. He, Y. Jin, F. Ding, L. Yang, Y. Ye, S. Zhong, Y. Lin, S. He, *Laser Photonics Rev.* **2014**, *8*, 495.
[33] T. Søndergaard, J. Jung, S. I. Bozhevolnyi, G. Della Valle, *New J. Phys.* **2008**, *10*, 105008.
[34] P. Hosseini, C. D. Wright, H. Bhaskaran, *Nature* **2014**, *511*, 206.
[35] C. Ríos, P. Hosseini, R. A. Taylor, H. Bhaskaran, *Adv. Mater.* **2016**, *28*, 4720.
[36] B. Broughton, L. Bandhu, C. Talagrand, S. Garcia-Castillo, M. Yang, H. Bhaskaran, P. Hosseini, *SID Symp. Dig.Tech. Pap.* **2017**, *48*, 546.
[37] S. Yoo, T. Gwon, T. Eom, S. Kim, C. S. Hwang, *ACS Photonics* **2016**, *3*, 1265.
[38] A. K. U. Michel, D. N. Chigrin, T. W. W. Maß, K. Schönauer, M. Salinga, M. Wuttig, T. Taubner, *Nano Lett.* **2013**, *13*, 3470.
[39] A.-K. U. Michel, P. Zalden, D. N. Chigrin, M. Wuttig, A. M. Lindenberg, T. Taubner, *ACS Photonics* **2014**, *1*, 833.
[40] E. Gourvest, B. Pelissier, C. Vallée, A. Roule, S. Lhostis, S. Maitrejean, *J. Electrochem. Soc.* **2012**, *159*, H373.
[41] K. Shportko, S. Kremers, M. Woda, D. Lencer, J. Robertson, M. Wuttig, *Nat. Mater.* **2008**, *7*, 653.
[42] B. Gholipour, A. Karvounis, J. Yin, C. Soci, K. F. MacDonald, N. I. Zheludev, *NPG Asia Mater.* **2018**, *10*, 533.
[43] S. Mukherjee, N. Smith, M. Goulding, C. Topping, S. Norman, Q. Liu, L. Kramer, S. Kularatne, J. Heikenfeld, *J. Soc. Inf. Disp.* **2014**, *22*, 106.
[44] J. Heikenfeld, P. Drzaic, J.-S. Yeo, T. Koch, *J. Soc. Inf. Disp.* **2011**, *19*, 129.
[45] https://www.idealliance.org/swop (accessed: March 2019).
[46] Y.-Y. Au, H. Bhaskaran, C. D. Wright, *Sci. Rep.* **2017**, *7*, 9688.
[47] A. Athmanathan, M. Stanisavljevic, N. Papandreou, H. Pozidis, E. Eleftheriou, *IEEE J. Emerging Sel. Top. Circuits Syst.* **2016**, *6*, 87.
[48] G. J. Lee, C. Choi, D.-H. Kim, Y. M. Song, *Adv. Funct. Mater.* **2017**, 1705202.
[49] A. T. Chuang, C. E. Margo, P. B. Greenberg, *Brit. J. Ophthalmol.* **2014**, *98*, 852.